RSC Advances

ROYAL SOCIETY OF CHEMISTRY

www.rsc.org/advances

RSC Advances

ARTICLE

Three-dimensionally ordered macroporous $LaMnO_3$ with tunable oxygen vacancies via nitric acid–aided modulating and their catalytic combustion properties

Received 00th January 20xx,
Accepted 00th January 20xx

DOI: 10.1039/x0xx00000x

www.rsc.org/

Renchun Yang*, Xiaojia Lu, Zhihua Zhang, Xiuxiang Wang, Dingxing Tang, Lingting Zhu

Three-dimensionally ordered macroporous (3DOM) $LaMnO_3$ oxides with tunable oxygen vacancies have been successfully fabricated via a facile nitric acid–aided modulating Sol-Gel method. The morphology, composition, pore structure and reducibility of the prepared catalysts were characterized by XRD, EDS, FE–SEM, XPS, TPR, and N_2 adsorption–desorption. The results indicate that the oxygen vacancies contents of the as-prepared catalysts are heavily dependent on the amount of nitric acid. Among the three $LaMnO_3$ catalysts, the $LaMnO_3$-C sample shows the highest oxygen vacancies content and the better low-temperature reducibility. These findings reveal that the introduction of a little amount of nitric acid can effectively promote the formation of oxygen vacancies, ultimately resulting in an enhanced catalytic oxidation activity for ethyl acetate oxidation.

1. Introduction

Over the past few years, the increasing appeals for limiting the volatile organic compounds (VOCs) emission were put forward owing to that most of them are harmful to human health and ecological security [1-3]. To efficiently remove VOCs, various technologies, such as adsorption, membrane separation, thermal combustion and catalytic oxidation are developed [4-6]. Among these methods, catalytic oxidation is considered as one of the most promising techniques for elimination of VOCs emissions due to its low operation temperature, low energy consumption and high removing efficiency [7-9]. To implement the catalytic oxidation preferably, the development of high-performance catalyst is necessary.

Among the catalysts investigated so far, supported noble metal catalysts were considered to be very efficient for catalytic oxidation of numerous VOCs. However, the high cost limits their wide applications. Thus, transition metal catalysts have attracted more attention. Among all the studied metal oxides, perovskite-type metal oxides, more especially $LaMnO_3$-based perovskites, are one type of environmentally friendly and relatively high active catalysts for VOC combustion [10-12]. Recent studies show that the three-dimensional-ordered macroporous (3DOM) materials with unique porous architecture and surface areas have attracted much attention due to their potential catalytic applications [13-15]. Thereby, lots of $LaMnO_3$ catalytic materials with 3DOM structure were developed for the VOC catalytic combustion and exhibited excellent catalytic performance [16-18]. It is well known that the catalytic performances of the catalysts are affected not only by their pore structure but also by their surface microstructures. Thus, much effort has been focused on varying the surface structure of $LaMnO_3$, such as surface chemical composition, reducibility, and oxygen vacancies, etc.

Oxygen vacancies, as one type of specific microstructures, have been demonstrated to have crucial effects on the physical and chemical properties of catalysts [19-21]. More importantly, recent studies indicate that the resulted unsaturated structure of oxygen vacancies can effectively reduce the activation energy of oxygen and improve the rate of catalytic oxidation, ultimately resulting in an enhanced catalytic performance [22,23]. Therefore, much effort has been devoted to design the oxygen vacancies. For constructing oxygen vacancies, one of the prevalent strategies is the substitution of lattice oxygen via introducing a foreign species, such as doping some metallic and non-metallic elements [24-26]. However, the resulted oxygen vacancies are often relatively limited. Thus, to obtain more oxygen vacancies, another popular approach for generating oxygen vacancies is the heat treatment of catalytic material in a vacuum system or a reducing atmosphere [27,28]. Clearly, most of these methods often need relatively rigorous conditions and complicated equipments, such as high temperature and high pressure. Therefore, it should be valuable to construct the oxygen vacancies via a facile method.

Motived by the above mentioned question, a facile nitric acid–aided modulating Sol-Gel method was explored to modulate the oxygen vacancies in this work. By controlling the little amount of nitric acid, the 3DOM $LaMnO_3$ composites with tunable oxygen vacancies contents were successfully achieved. The process is facile and low-cost since only little amount of nitric acid was introduced in the preparation process

School of Biological and Chemical Engineering, Anhui Polytechnic University, Wuhu, 241000, P. R. China. E-mail: yrclq@163.com; Fax: +86-553-2871255

of $LaMnO_3$ and without adding any other material or complex program. The effects of nitric acid amount on the structure of 3DOM $LaMnO_3$ were investigated in detail. Moreover, the catalytic oxidation properties of the resulted $LaMnO_3$ composites on ethyl acetate (EA) were tested.

2. Experimental

2.1. Synthesis of polystyrene spheres (PS) colloidal crystal template

All chemicals used were of analytical grade. Firstly, colloidal crystal templates were synthesized by preparing polystyrene spheres with about 280 nm diameter via emulsifier-free emulsion polymerization. In a typical synthesis, a given amount of styrene with an equal volume 5% wt NaOH were added repeatedly to a separatory funnel to ensure that no colour can be found in the water layer. Then, a given amount of the styrene (6.0 mL), Sodium p-Styrene Sulfonate (NaSS, 21 mg), Potassium persulfate (KSP, 42 mg) and deionized water (53.0 mL) were stirred together in a five-neck round-bottom flask to form an emulsion under N_2 protection. The polymerization was conducted at 70 °C under mechanical stirring for 12 h. After polymerization, the spheres were close-packed into colloidal crystals by centrifugation (2500 rpm, 12 h) followed by drying at room temperature.

2.2. Synthesis of 3DOM $LaMnO_3$

The 3DOM $LaMnO_3$ samples with tunable oxygen vacancies were prepared using the nitric acid-assisted strategy. In a typical procedure, 0.5004 g of jiusuan, 0.4 g of P123 and 0.75 mL nitric acid were firstly dissolved in one beaker with 5.5 mL of ethanol at room temperature; the resulted solution is named sample A. Then, the 0.002 mmol of $Cu(NO_3)_2 \cdot 3H_2O$ and 0.002 mmol of $La_2(NO_3)_3$ were dissolved in another beaker with 6.0 mL of ethanol; the solution is named sample B. Subsequently, the sample A was added into the sample B with vigorous stirring for 30 second. Then, the mixed solution was infiltrted into the colloidal crystal templates in a closed glass vessel and dried at ambient temperature under vacuum for 12 h. After that, the sample was calcined at 750 °C in air for 3 h. The resultant sample was designated LaMnO3-A. To study the effects of the amount of nitric acid on the structure of the $LaMnO_3$, the other two samples were also prepared with the amount of nitric acid at 8.5 mL and 9.5 mL and keeping other conditions unchanged, which are named as $LaMnO_3$-B and $LaMnO_3$-C, respectively.

2.3. Characterization of samples

X-ray Diffraction patterns of the samples were obtained with a Rigaku diffractometer/MAX-RB by nickel-filtered Cu Kα radiation (λ=154.056 pm). Diffraction patterns were recorded over a range of 2θ angles from 20° to 80° using a 0.02° step size. The morphology of the as-prepared samples was characterized using a scanning electron microscope (FE–SEM, Hitachi S4800). The porosity characteristics of the catalysts were determined by nitrogen adsorption–desorption (NOVA 2000e). BET (Brunauer–Emmett–Teller) surface areas of the samples were measured via N_2 adsorption at -196 °C with the samples outgassed at 300 °C for 2 h under vacuum before measurement. Thermo ESCALAB 250 XPS Spectrometer, with Al Kα radiation, was used for obtaining XPS data. In XPS study, C 1s-binding energy value of 285 eV was taken as a reference level. Temperature programmed reduction (TPR) measurements were carried out in a TPDRO 1100 series (Thermo electron corporation) instrument. About 50 mg of catalyst was placed in a U-shaped quartz sample tube. Prior to TPR studies, each catalyst sample was pretreated in an inert gas (N_2, 30 mL/min) at 200 °C for 1 h. After pretreatment, the sample was cooled to ambient temperature and the carrier gas consisting of 5% hydrogen balance argon (30 mL/min) was allowed to pass over the sample; the temperature was increased from ambient to 930 °C at a heating rate of 10 °C/min.

2.4 Catalytic testing

Catalytic oxidation reactions were performed in a continuous-flow system at atmospheric pressure. A stainless tube of 6 mm of inner diameter was filled with 200 mg catalyst diluted with 1.5 g quartz sand to ensure a homogeneous thermal distribution. The experiments were carried out at atmospheric pressure and the gas hourly space velocity (GHSV) was maintained at 15,000 h^{-1}. The liquid EA feed and the dry air were input by a HPLC pump and a mass flow controller, respectively. The injection point of EA was electrically heated to ensure complete evaporation of the liquid reaction feeds. The concentration of EA in the reaction feeds was set at 1000 ppm. The effluent gases were analyzed by an on-line gas chromatograph equipped with a FID detector.

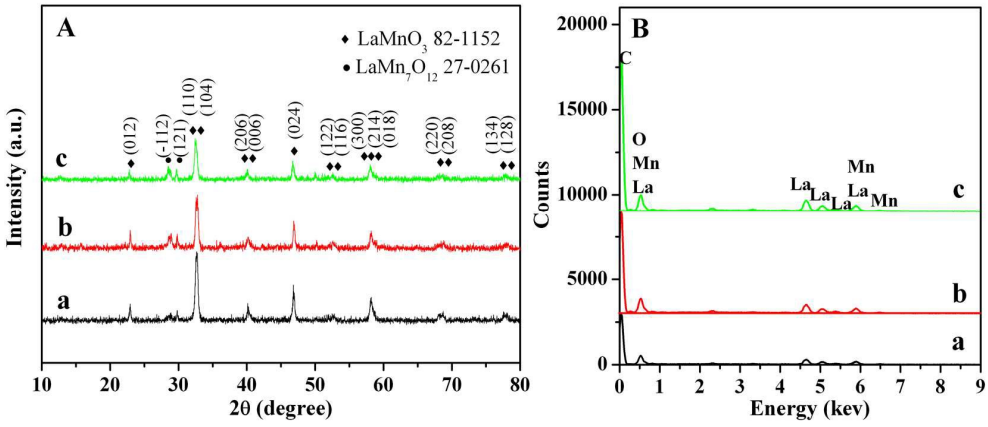

Fig. 1. (A) XRD patterns and (B) EDS spectrum of the samples: (a) $LaMnO_3$-A, (b) $LaMnO_3$-B and (c) $LaMnO_3$-C.

RSC Advances

ARTICLE

3. Results and discussion

3.1 XRD and EDS analysis

Fig. 1A shows the XRD patterns of the resultant samples. As can be seen, one obvious characteristic is that the three samples all exhibited similar reflection peaks, indicating that the samples holding similar composes. By referring to the XRD pattern of standard $LaMnO_3$ sample (JCPDS 82-1152), one can deduce that the three catalysts are all single-phase with rhombohedral crystal structure. Moreover, the two faintness peaks around 30° should be attributed to the (-112) and (121) of phases of the $LaMn_7O_{12}$ (JCPDS 27-0261). It seems that the crystallite structure of the $LaMnO_3$ is not affected by the added nitric acid. However, based on observing carefully, one can find that the distinct difference existed for the three samples of their peak widths. Generally, the peak width of XRD patterns is closed to its crystallite size. Thus, to study the size of particles, the single peak of $LaMnO_3$ at $2\theta = 46.87°$ were calculated based on Scherrer's equation; results are shown in Table 1. From the calculated results, the estimated average crystallite sizes were 22 nm for $LaMnO_3$-A, 20 nm for $LaMnO_3$-B, and 18 nm for $LaMnO_3$-C. It can be found that the crystallite size of the three samples follows the order: $LaMnO_3$-A > $LaMnO_3$-B > $LaMnO_3$-C. Thus, a suitable increase of the nitric acid amount should be helpful to obtaining some smaller $LaMnO_3$ particles.

Fig. 1B shows the EDS element analysis of as-prepared catalysts. As can be seen, the three samples all include four elements (La, Mn, O, and C). Among them, the signal of C should be ascribed to the anisotropic conductive film, while the signals of La, Mn, and O are attributed to the $LaMnO_3$ samples. From the Table 1, one can find that three samples exhibit a similar La:Mn:O atomic ratio, confirming that the foregoing XRD analysis that the samples possess similar chemical composes. From the XRD and EDS analysis, one can speculate that that the addition of little amount nitric acid can promote the formation of $LaMnO_3$ with small particle but not influence its crystallite composes.

Table 1 Textural properties of various samples

Sample	XRD	EDS	N_2 adsorption-desorption			XPS	
	Crystallite size (nm)	La:Mn:O atomic ratio	BET surface Area (m^2 g^{-1})	Pore volume (cm^3 g^{-1})	Average pore size (nm)	Mn^{3+}/Mn^{4+} atomic ratio	O_{ads}/O_{latt} atomic ratio
$LaMnO_3$-0.75	22	20.9:20.5:58.6	9.5	0.041	28	1.21	1.56
$LaMnO_3$-0.85	20	21.2:20.9:57.9	12.3	0.069	21	0.94	1.7
$LaMnO_3$-0.95	18	21.6:21.4:57.0	15.2	0.075	18	0.78	1.94

3.2 Morphology characterization

The morphology of the samples was characterized by SEM and the results are showed in Fig. 2. To study the effect of nitric acid on the samples, a series of experiments have been carried out by only changing the amount of nitric acid and keeping other conditions unchanged. As can be seen, the amount of nitric acid plays a very crucial role on controlling the morphologies of $LaMnO_3$ composites. When the adding amount of nitric acid is 0.95 mL, highly ordered porous structure in three dimensions can be found in the product (Fig. 2a-1,2). The average macropore size and wall thicknesses of the samples are around 150 nm and 30 nm, respectively. The next layer pore and porous walls can also be easily found, suggesting that the resulted samples are an open interconnected 3DOM macroporous network. With the decrease of nitric acid amount to 0.85 mL, similar morphology and porous structure present for the $LaMnO_3$-B (Fig. 2b-1,2). However, compared with the $LaMnO_3$-C sample, the $LaMnO_3$-B sample shows a relatively low ordered for the porous structure. Further decrease of the amount of nitric acid to 0.75 mL, only some particles with the size about 50-100 nm can be observed (Fig. 2a-1,2). Distinctly, no 3DOM macroporous network can be observed for the $LaMnO_3$-A sample.

Such result should be ascribed to the formation ratio of $LaMnO_3$ colloid. Obviously, the formation of the 3DOM macroporous network need filling the colloidal crystal template with some small colloid particles. Relative big colloid particles must be prevented outside and cannot enter into the interval of the colloidal crystal template, which is not beneficial to the constructing of 3DOM structure. From the three samples, one can deduce that the higher the amount of nitric acid was offered, the smaller the size of the $LaMnO_3$ colloid particles presented, which is also confirmed by foregoing XRD analysis. In fact, in our exploring experiment, we found that the colloid generated immediately when no nitric acid was introduced, whereas no colloid occurred within the monitoring period (two weeks) as the addition amount of nitric acid bigger than 1.0 mL. Such phenomenon should be due to that the introduction of nitric acid inhibits the ionization of tartaric acid and then decreases the contacting rate of the tartaric acid ions and the metallic cations. Thus, the introduction of little amount of nitric acid is helpful to obtaining the $LaMnO_3$ sample with 3DOM structure.

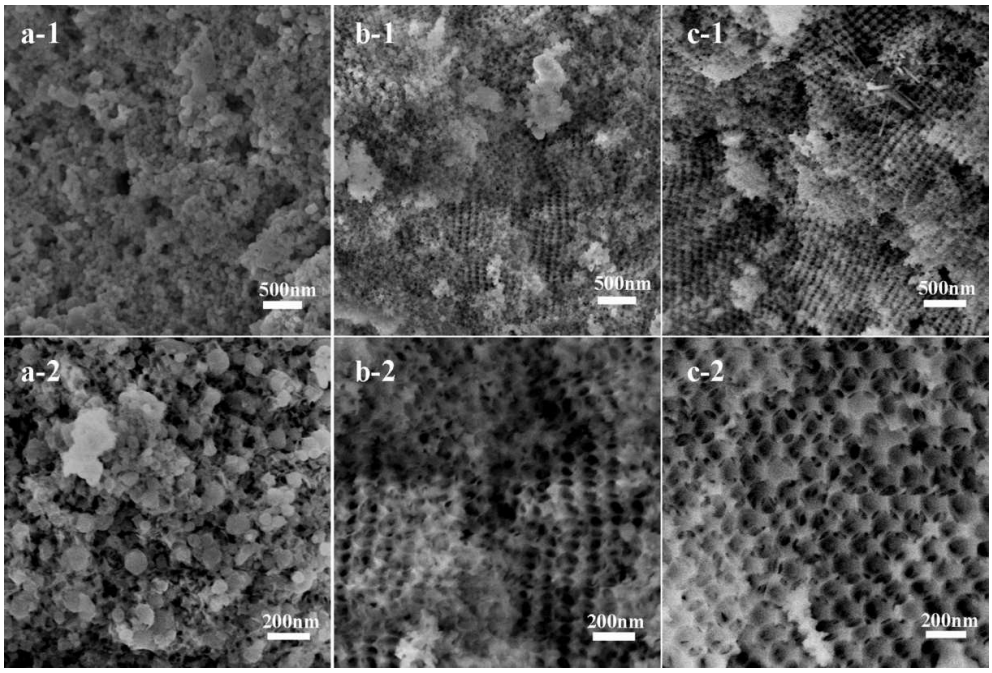

Fig. 2. SEM images of the samples: (a-1,2) $LaMnO_3$-A, (b-1, 2) $LaMnO_3$-B, (c-1,2) $LaMnO_3$-C.

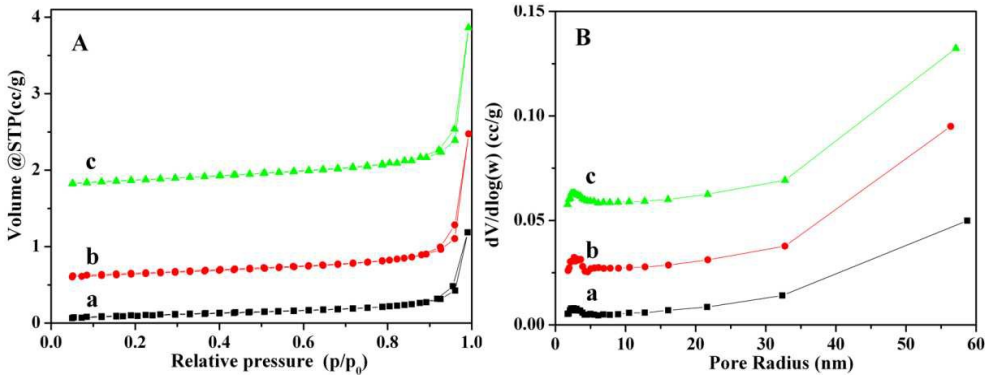

Fig. 3. (A) Nitrogen adsorption-desorption isotherm and (B) pore-size distributions of the samples: (a) $LaMnO_3$-A, (b) $LaMnO_3$-B and (c) $LaMnO_3$-C.

3.3 Textural analysis

Fig. 3 shows the N_2 adsorption–desorption isotherms and pore size distributions of the $LaMnO_3$ samples prepared under different amount of nitric acid, and their BET surface areas and pore properties are summarized in Table 1. As can be seen in Fig. 3A, isotherms for the as-made samples are of type II with a type H3 hysteresis loop, indicating that the existence of macropores [29,30]. The pore size distribution for these samples indicates that some mesoporous with relative broad size distribution (around 30 to 60 nm) also exist within the resulted samples (Fig. 3B). Additionally, for all samples, there was also presence of a small amount of micropores with an intense peak in the range of 2.0–4.0 nm. As can be seen in Table 1, the specific surface areas of the samples $LaMnO_3$-A, $LaMnO_3$-B, $LaMnO_3$-C are 8.3, 12.3 and 14.1 $m^2\ g^{-1}$, respectively. The pore volume of the samples $LaMnO_3$-A, $LaMnO_3$-B, $LaMnO_3$-C are 0.041, 0.069 and 0.075 $cm^3\ g^{-1}$, respectively. Obviously, the introduction of a certain amount of nitric acid is beneficial to obtaining relatively large specific surface area and pore volume. Such result should be ascribed to that the colloid particles with small size is helpful to enhancing the surface area, which is consisted with the foregoing analysis that the smaller colloid particles can easily form as the introducing of little nitric acid.

3.4 XPS analysis

More detailed information about the chemical composition, surface electronic state and oxygen vacancy of the samples was acquired from XPS; results are shown in Fig. 4. The spectra a, b and c profiles represent the samples $LaMnO_3$-A, $LaMnO_3$-B and $LaMnO_3$-C, respectively. Fig. 4A shows the Mn 2p3/2 region of the X-ray photoelectron spectra. As can be seen, the three samples all exhibit a typical Mn 2p3/2 XPS spectrum with two peaks with maximum at 641.5 and 643.0 eV, which are assigned to the Mn^{3+} species and the Mn^{4+} species, respectively [31]. O 1s XPS spectra of the three samples are shown in Fig. 4B. The spectra of the three samples all show two peaks around at 529.2 and 531.5 eV. It is reported that the characteristic line at 530.5 eV was attributed to surface lattice oxygen (O_{latt}) species, whereas the peak located at 531.5 eV was ascribed to the adsorbed oxygen (O_{ads}) species [17,32].

Through preliminary observation, one can found that some difference about the surface Mn^{4+}/Mn^{3+} and O_{ads}/O_{latt} peak area ratios exist for the $LaMnO_3$ samples. Thus, peak areas of the recorded spectra were estimated by fitting the curves with combination of Gaussian curves of variable proportion [33]. The results about the surface element compositions for the Mn^{4+}/Mn^{3+} and O_{ads}/O_{latt} ratios are given in Table 1. As can be seen, with the increase of nitric acid amount, the Mn4+/Mn3+ and O_{ads}/O_{latt} ratios of the three samples all follows the order: $LaMnO_3$-A < $LaMnO_3$-B < $LaMnO_3$-C. Obviously, the $LaMnO_3$-C sample not only holds the highest Mn^{4+}/Mn^{3+} value (1.28) but also presents the highest O_{ads}/O_{latt} molar ratio (1.94), indicating that higher nitric acid content is beneficial to the enhancement of surface Mn^{4+} species and O_{ads} oxygen species. It is generally accepted that O_{ads} oxygen species are mainly influenced by surface oxygen vacancies for the oxide catalysts [33,34] since they are often adsorbed only by the oxygen vacancies at vacuum conditions. Thus, more oxygen vacancies should occur on the sample with higher O_{ads} species content, which are responsible for the higher activity of catalysis [24]. From the above analysis, one can conclude that the introduction of a certain amount of nitric acid can promote the increase of oxygen vacancies content.

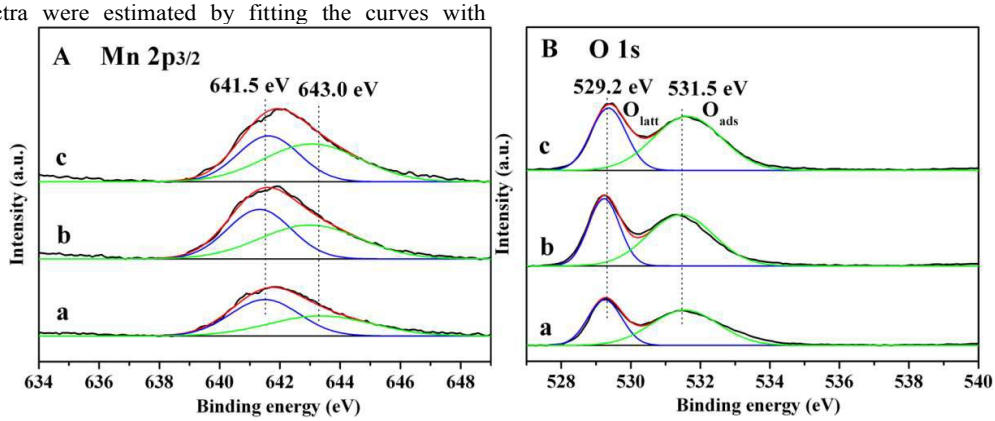

Fig. 4. (A) Mn 2p3/2 and (B) O 1s XPS spectra of the samples: (a) $LaMnO_3$-A, (b) $LaMnO_3$-B and (c) $LaMnO_3$-C.

3.5 Surface oxygen species and reducibility

The TPR characterization is often used to analyze the reducibility and surface species for the metal oxide catalysts [35-37]. To investigate the effects of the addition amount of nitric acid on the surface oxygen species and reducibility, we characterized the three samples by TPR; results are shown in Fig. 5. Clearly, the reduction process of each sample underwent in two steps: one in the range of 300–620 °C and the other in the range of 620–900 °C. More importantly, the low temperature range includes two reduction peaks, while the high temperature range is consisted of three reduction peaks. According to relative reports [38], we know that the first present reduction peaks at 415–452 °C should be ascribed to the reduction of Mn^{4+} to Mn^{3+} as well as the adsorption oxygen species, and the reduction peaks at 478–587 °C to the reduction of Mn^{3+} with coordination-unsaturated compose, whereas the reduction peaks above 620 °C were attributed to the reduction of the Mn^{3+} to Mn^{2+} [39,40]. The adsorption oxygen species and the coordination-unsaturated oxygen species are often corresponding to the oxygen vacancies, which not only are easier to be reduced but also possess more chances to act as active sites. Thus, increasing the proportion of the low temperature step should be an effective way to enhance the content of oxygen vacancies and then increase the number of active sites.

As shown in Fig. 5, the addition amount of nitric acid caused two types of effects on the TPR profiles of the $LaMnO_3$ catalysts. One is the position of the reduction peaks, the other is the intensity of every reduction peaks. Generally, the position of reduction peak represents one type of specific oxygen species of the $LaMnO_3$, and the intensity of reduction peaks represents the content of the oxygen species. According to forgoing analysis, we know that the position of low temperature reduction step (corresponding to oxygen vacancies) is more related to the catalytic activity. Moreover, the catalytic oxidation at low temperature is more useful than that of at high temperature in practical applications. Thus, we especially focus on the low temperature peaks of H_2–TPR (below 620 °C).

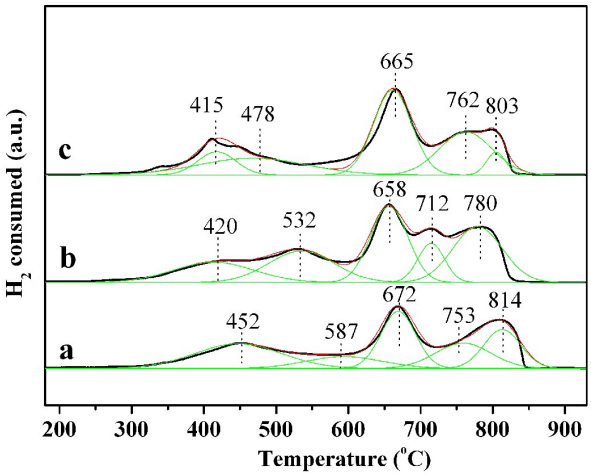

Fig. 5. H_2-TPR profiles of samples: (a) $LaMnO_3$-A, (b) $LaMnO_3$-B and (c) $LaMnO_3$-C.

Firstly, for the peaks positions: if one compare the temperatures, one can find that the two low temperature peaks all follow the order: $LaMnO_3$-C (415 and 478 °C) < $LaMnO_3$-B (420 and 532 °C) < $LaMnO_3$-A (452 and 587 °C). According to the routine analysis, the reduction temperature should be affected by the metal to oxygen bond-energy. Obviously, the stronger the bond-energy is, the higher the reduction temperature is. Among the three samples, the $LaMnO_3$-C holds the peak with the lowest reduction temperature, suggesting that the introduction of a certain amount of nitric acid for $LaMnO_3$ can promote the low temperature catalytic oxidation reaction. Secondly, for the peaks intensities: to quantitative analysis the peaks intensities, each peak was estimated by fitting the curves with a combination of Gaussian curves of variable proportion; results are summarized in Table 2. Since the reduction temperature of the second peak (478 °C) for the $LaMnO_3$-C sample is distinctly lower than those of the other samples ($LaMnO_3$-A and $LaMnO_3$-B), the peak was integrated into the lowest temperature reduction peak for the $LaMnO_3$-C sample. Distinctly, compared with the $LaMnO_3$-A and $LaMnO_3$-B, the $LaMnO_3$-C exhibited the highest proportion of H_2 consumed for the low temperature reduction peak. From the analysis of the peak position and peak intensity, we can conclude that the introduction of a certain amount of nitric acid for $LaMnO_3$ is helpful to enhancing the content of oxygen vacancies and decreasing the catalytic oxidation temperature.

Table 2 The results of quantitative analysis from H_2-TPR profiles

Sample	Peak area/ Total area and temperature of peak maximum (◦C)					
	T < 500	$T_{p,m}$	500 < T < 700	$T_{p,m}$	T > 700	$T_{p,m}$
$LaMnO_3$-A	21%	452	43%	587,672	36%	753, 814
$LaMnO_3$-B	19%	420	44%	532,658	37%	712,780
$LaMnO_3$-C	32%	415,478	37%	665	31%	762,803

3.6 catalytic performance

To evaluate the as-synthesized samples, the catalytic oxidation conversion of ethyl acetate as a function of the temperature was used to monitor the catalytic properties; results are shown in Fig. 6. As can be seen in Fig. 6A, the conversion of ethyl acetate monotonously increased with an increase in the reaction temperature, and a complete conversion of ethyl acetate could be successfully achieved below 400 °C over all samples. Moreover, there are exist distinct difference for the transformation temperature of the three samples. For the $LaMnO_3$-C, the conversion starts at about 140°C and it is completed below 340°C, while for the $LaMnO_3$-A and $LaMnO_3$-B the conversion start at similar temperatures but it is completed at 360 and 400 °C, respectively. Clearly, at the identical conversion, the reaction temperature of the $LaMnO_3$-C is clearly lower than the $LaMnO_3$-A and $LaMnO_3$-B, suggesting that the catalytic performance of the $LaMnO_3$-C is superior to those of $LaMnO_3$-A and $LaMnO_3$-B at the similar reaction temperature. To furtherer compare the catalytic activities of the samples, the conversions at T_{10}, T_{50} and T_{90}, corresponding to the temperatures at 10, 50 and 90% of conversion, respectively, are used and are summarized in Table 3. Clearly, the $LaMnO_3$-A showed the optimum catalytic activity for ethyl acetate oxidation with the T_{10}, T_{50} and T_{90} of 180, 225 and 260 °C, respectively, which were lower than those of the samples $LaMnO_3$-A and $LaMnO_3$-B. Obviously, the conversion of ethyl acetate follows the order: $LaMnO_3$-A < $LaMnO_3$-B < $LaMnO_3$-C. Such order is consisted with that of the oxygen vacancies content of the three samples, indicating that the oxygen vacancies content play an important role for their catalytic performance. Moreover, the performance of $LaMnO_3$-B and $LaMnO_3$-C are higher than $LaMnO_3$-A, suggesting that the 3DOM structure maybe helpful to increasing the mass transfer efficiency.

To evaluate the catalytic stability of the samples for ethyl acetate oxidation, a durability test over each sample was carried out for 10 h at the reaction temperature of 280 °C; the curves of conversion versus time on stream are shown in Fig. 6B. As can be seen, no obvious decrease of catalytic activity was observed for all samples after 10 h testing. Distinctly, the $LaMnO_3$-C not only exhibited the best catalytic activity but also presented a good stability, suggesting that the as-prepared sample is a stable catalyst under these reaction conditions.

RSC Advances

ARTICLE

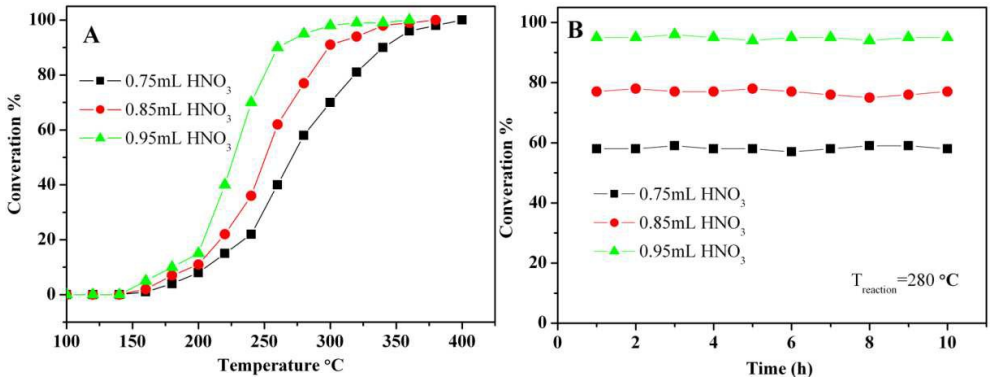

Fig. 6. (A) The catalytic combustion performance and (B) catalytic stability of samples: (a) $LaMnO_3$-A, (b) $LaMnO_3$-B and (c) $LaMnO_3$-C.

Table 3 Temperatures for 10%, 50% and 90% of conversion in the catalytic oxidation of EA

Sample	T_{10} (°C)	T_{50} (°C)	T_{90} (°C)
$LaMnO_3$-A	205	270	340
$LaMnO_3$-B	195	250	295
$LaMnO_3$-C	180	225	260

4. Conclusions

In summary, three-dimensionally ordered macroporous $LaMnO_3$ with tunable oxygen vacancies have been successfully fabricated via a simple nitric acid–aided method. The effects of the nitric acid amount on their structure and catalytic properties were investigated in detail. The results indicate that the two significant influence factors (oxygen vacancies content and reducibility) for the as-prepared samples are heavily dependent on the amount of nitric acid. Among the three $LaMnO_3$ catalysts, the $LaMnO_3$-C sample presented the highest catalytic activity for ethyl acetate oxidation, which should be attributed to its higher oxygen vacancies content and better low-temperature reducibility. This study provides a promising route to fabricate the 3DOM $LaMnO_3$ composite with tunable oxygen vacancies and high catalytic oxidation activity for acetate oxidation.

Acknowledgements

This work is supported by National Nature Science Foundation of China (51572004 and 51202003).

References

1 L. Wang, H. Zhang, Y, Yan and X. Zhang, *RSC Adv.*, 2015, **5(37)**, 29482–29490.
2 X. Liu, J. Wang, J. Zeng, X. Wang and T. Zhu, *RSC Adv.*, 2015, **5(64)**, 52066–52071.
3 A. M. Carrillo and J. G. Carriazo. *Appl. Catal. B: Environ.*, 2015, **164**, 443–452.
4 H. K. Son, S. Sivakumar, M. J. Rood and B. J. Kim, *J. Hazard. Mater.*, 2016, **301**, 27–34.
5 J. Kujawa, S. Cerneaux and W. Kujawski, *J. Membrane Sci.*, 2015, **474**, 11–19.
6 J. Leclercq, F. Giraud, D. Bianchi and F. Gaillard, *Catal. Commun.*, 2015, **67**, 35–39.
7 M. H. Castaño, R. Molina and S. Moreno, *Appl. Catal. A: Gen.*, 2015, **492**, 48–59.
8 M. Piumetti, D. Fino and N. Russo, *Appl. Catal. B: Environ.*, 2015, **163**, 277–287.
9 Y. Wu, X. Liu, X. Huang, S. Xing, Z. Ma and L. Feng, *Mater. Lett.*, 2015, **139**, 157–160.
10 C. Zhang, Y. Guo, Y. Guo, G. Lu, A. Boreave, L. Retailleau, A. Baylet and A. Giroir-Fendler, *Appl. Catal. B: Environ.*, 2014, **148**, 490–498.

11 Y. Lu, Q. Dai ad X. Wang, *Catal. Commun*., 2014, **54**, 114–117.
12 S. Chen, Y. Wang, A. Jia, H. Liu, M. Luo and J. Lu, *Appl. Surf. Sci*., 2014, **307**, 178–188.
13 X. Yu,, Z. Zhao, Y. Wei, J. Liu, J. Li, A. Duan and G. Jiang, *RSC Adv*., 2015, **5**, 49780–49790.
14 J. Ma, Y. Ning, C. Gong, G. Xue and G. Fana, *RSC Adv*., 2015, **5**, 53441–53447.
15 H. Kim, H. S. Lim, Y. J. Kim, Y. K. Sun and K. D. Suh, *RSC Adv*., 2014, **4**, 60573–60580.
16 Y. Liu, H. Dai, J. Deng, Y. Du, X. Li, Z. Zhao, Y. Wang, B. Gao, H. Yang, G. Guo, *Appl. Catal. B: Environ*., 2013, **140**, 493–505.
17 Y. Liu, H. Dai, Y. Du, J. Deng, L. Zhang, Z. Zhao, C. T. Au, *J. Catal*., 2012, **287**, 149–160.
18 M. Sadakane, K. Sasaki, H. Nakamura, T. Yamamoto, W. Ninomiya and W. Ueda, *Langmuir*, 2012, **28(51)**, 17766–17770.
19 T. T. Chen, I. C. Chang, M. H. Yang, H. T. Chiu and C. Y. Lee, *Appl. Catal. B: Environ*., 2013, **142–143**, 442–449.
20 K.Y. Lee and Y. J. Huang, *Appl. Catal. B: Environ*., 2014, **150–151**, 506–514.
21 Q. Wu and R. van de Krol, *J. Am. Chem. Soc*., 2012, **134**, 9369–9375.
22 Z. H. Wei, J. M. Sun, Y. Li, A. K. Datyec and Y. Wang, *Chem. Soc. Rev*., 2012, **41**, 7994–8008.
23 M. Li, Y. Hu, S. Xie, Y. Huang, Y. Tong and X. Lu, *Chem. Commun*., 2014, **50**, 4341–4343.
24 X. Chen, L. Liu, P. Y. Yu and S. S. Mao, *Science*, 2011, **331**, 746–750.
25 F. Cheng, T. Zhang, Y. Zhang, J. Du, X. Han and J. Chen, *Angew. Chem. Internat. Edit*., 2013, **52**, 2474–2477.
26 M. Samiee and J. Luo, *Mater. Lett*., 2013, **98**, 205–208.
27 Q. Wu and R. van de Krol, *J. Am. Chem. Soc*., 2012, **134(22)**, 9369–75.
28 J. Y. Shin, J. H. Joo, D. Samuelis and J. Maier, *Chem. Mater*., 2012, **24(3)**, 543–551.
29 F. Kleitz, F. Bérubé, R. Guillet-Nicolas, C. Yang and M. Thommes, *J. Phys. Chem. C*, 2010, **114**, 9344–9355.
30 R. Yang, L. Yang, T. Tao, F. Ma, M. Xu, Z. Zhang, *Appl. Surf. Sci*., 2014, **288**, 363–368.
31 H. B. Deng, L. Lin, Y. Sun, C. S. Pang, J. P. Zhuang, P. K. Ouyang, Z. J. Li, S. J. Liu, *Catal. Lett*., 2008, **126**, 106–111.
32 A. Machocki, T. Ioannides, B. Stasinska, W. Gac, G. Avgouropoulos, D. Delimaris, W. Grzegorczyk and S. Pasieczna, *J. Catal*., 2004, **227**, 282–296.
33 J. H. Scofield, *J. Electr, Spectrosc. Relat. Phenom*., 1976, **8**, 129–137.
34 B.P. Barbero, J.A. Gamboa and L.E. Cadús, *Appl. Catal. B: Environ*., 2006, **65**, 21–30.
35 Y. Zhu, Y. Sun, X. Niu, F. Yuan and H. Fu, *Catal. Lett*., 2010, **135**, 152–158.
36 T. Borowiecki, W. Gac and A. Denis, *Appl. Catal. A: Gen*., 2004, **270**, 27–36.
37 H. H. Lu, H. B. Yin, Y. M. Liu, T. S. Jiang and L. B. Yu, *Catal. Commun*., 2008, **10**, 313–316.
38 L. L. Qu, W. P. Zhang, P. J. Kooyman and R. Prins, *J. Catal*., 2003, **215**, 7–13.
39 Y. Liu, H. Dai, Y. Du, J. Deng, L. Zhang, Z. Zhao, *Appl. Catal. B: Environ*., 2012, **119–120**, 20–31.
40 A. Kaddouri, S. Ifrah and P. Gelin, *Catal. Lett*., 2007, **119**, 237–244.
41 F. Teng, W. Han, S. H. Liang, B. Gaugeu, R. L. Zong, Y. F. Zhu, *J. Catal*., 2007, **250**, 1–11.

Graphical abstract